Mechanistic Insights into the Selective Targeting of MLX to Triacylglycerol-Rich Lipid Droplets

R. Jay Braun[1] and Jessica M. J. Swanson[1*]

[1]Department of Chemistry, University of Utah, Salt Lake City, UT 84112-0850, USA

*Corresponding author, j.swanson@utah.edu

Abstract:
The activation of transcription factor Max-Like Protein x (MLX) is modulated by competition between active dimerization and inactive association with cytosolic lipid droplets (LDs). However, LD association has been shown to depend on the neutral lipid composition. This work explores the mechanism by which MLX specifically targets LDs rich in triacylglycerol (TG) over those with abundant sterol esters (SE). We compare the association ensembles for a potential minimal targeting sequence—an amphipathic helix-loop-helix hairpin—and the full dimerization and cytoplasmic localization domain (DCD), finding the latter requires larger packing defects and induces quantifiable LD membrane alterations. Surprisingly, direct interactions with TG neutral lipids are not observed for either sequence. Instead, targeting to SE-rich LDs is blocked by insufficient packing defects. We additionally explore the full mechanism of hairpin association, aiming to understand sequence-specific features that enable strong association with TG-rich LD monolayer membranes. We find that there are multiple association pathways, but that each involves a catch, snorkeling, and burial phase. The combination of multiple catch residues placed on opposing ends of amphipathic helices lengthens the catch phase, greatly enhancing association in a manner that resembles kinetic selection. Once bound, locking interhelical interactions block dissociation. These findings suggest that in addition to relative binding affinities, both kinetics and altered surface properties upon protein association could influence competition within the LD proteome.

Significance:

The localization and activity of Max-Like Protein x (MLX), a cancer-relevant transcription factor, is controlled by competition between activating dimerization and inactivating association with lipid droplets (LDs). This work reveals how MLX selectively associates with LDs rich in triacylglycerol lipids while avoiding those rich in sterol esters and how a shorter hairpin from MLX binds to membranes broadly. A dynamic interplay between protein association and membrane monolayer properties explains targeting specificity and suggests that kinetic and allosteric regulation may influence competition within the LD proteome.

Introduction

Lipid Droplets (LDs) are cellular organelles that control lipid storage, distribution, and processing. In addition to their expected roles in lipolysis, lipogenesis, and the production of membrane building blocks, LDs have been found to play increasingly diverse roles (1–5), including in transcriptional regulation (6). Max like protein X (MLX) (Figures 1, S1 a) was the first transcription factor identified to associate with LDs (6). As a member of the MYC- and MAX-centered network of transcription factors, MLX forms a dimer using a basic helix-loop-helix-leucine architecture (Figure 1 a) that can bind DNA and influence expression levels. Unlike MYC and MAX, MLX has a small dimerization and cytoplasmic localization domain (DCD, Figure 1 b) that regulates its activity. When bound to one of its dimerization partners (another MLX in a homodimer (Figure 1 a) or MondoA or ChREBP as a heterodimer (Figure 1 c-d)) (7–9) MLX can translocate to the nucleus where it regulates the transcription of proteins involved in glucose metabolism (10–15). In the presence of LDs, however, MLX can be stalled in the cytosol for sustained periods due to the DCD association with the LD surface with a slow apparent off-rate (6). In this manner LD association alters MLX-driven gene expression, providing a link between lipid storage organelles and glucose metabolic regulation.

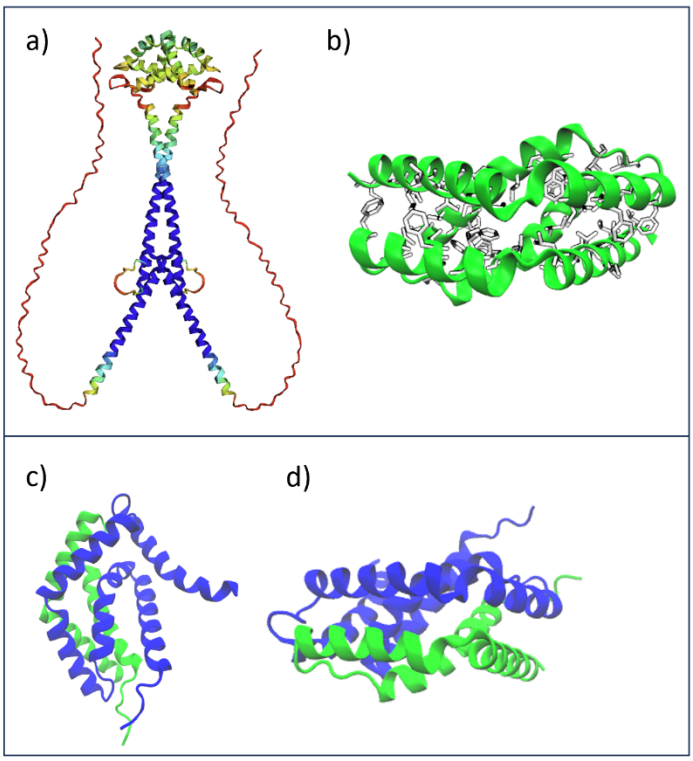

Figure 1. The predicted structures of a) the MLX homodimer, b) the homodimeric DCD, and the heterodimeric MLX-MondoA DCD from the c) top and d) side views.

LDs are uniquely characterized by a phospholipid (PL) monolayer membrane, unlike the bilayer membranes found in other organelles. This monolayer encapsulates a neutral lipid core primarily composed of triacylglycerols (TGs) and sterol-esters (SEs). Decorating the monolayer is a dynamic array of proteins, collectively known as the LD proteome, which facilitate diverse lipid-related processes (1, 2, 4, 5, 16, 17). Understanding how proteins selectively associate with LDs at different stages of their lifecycle is an emerging area of LD research. Proteins that migrate from the cytosol, traditionally referred to as class II and now termed cytosol to LD (CYToLD) proteins, target the LD monolayer via amphipathic helices (AHs). These helices embed into the numerous and large packing defects on the LD monolayer, where hydrophobic residues interact with the membrane's exposed hydrophobic PL-acyl tail or neutral lipid regions. Meanwhile, polar residues engage with water or polar PL-headgroups. Another group of proteins, formerly known as class I and recently designated ER to LD (ERtoLD) proteins, translocate from the endoplasmic reticulum (ER) to the LD

monolayer through membrane bridges. These proteins often feature membrane-embedded motifs, such as hairpins or longer U-shaped structures (2). In some cases, these motifs can possess polar or charged residues, which interact with ER-PL headgroups before engaging with the LD upon translocation. Together, these distinct protein classes regulate LD dynamics, including lipolysis, lipogenesis, and lipid trafficking—key facets of cellular lipid homeostasis.

LD proteomes have been shown to change in response to neutral lipid composition, with high TG or SE-compositions identified in distinct LD subpopulations (18–24). Although the physical origin of proteome remodeling is not fully understood, it has been proposed that the selective protein targeting to subpopulations is at least partially driven by the unique physical features of TG- vs SE-rich LDs (18). TG-rich LDs feature an amorphous core in which TG tails intercalate with the LD monolayer membrane, leading to larger and more frequent membrane packing defects (regions where the PL headgroups splay apart to expose hydrophobic acyl tails to water) (20, 25). Additionally, TG molecules can intercalate into the PL monolayer and adopt conformations similar to PL molecules with their glycerol group facing the cytosol and their acyl tails packing in with PL tails (20). These surface-active TGs (SURF-TGs) explain the ~15% increase in area per lipid headgroup measured experimentally (24) in LD monolayers compared to the endoplasmic reticulum (ER) bilayer, their site of origin with the same PL composition. They additionally create chemically distinct packing defects and, thus, LD-specific handles for proteins to target (2, 21, 26). SE-rich LDs differ substantially from their TG-rich counterparts, in part due to their propensity to undergo a phase transformation (22, 27). Under certain conditions (e.g., stress or starvation), SEs can transition into a liquid-crystalline smectic phase characterized by the formation of concentric rings beneath the PL monolayer (6, 19, 22, 27). Simulations have shown that this transformation increases the internal ordering of the droplet core and propagates outward to the monolayer, reducing the overall number of packing defects by ~50% (18). Furthermore, the denser PL packing expels SURF-TGs, thereby limiting opportunities for certain proteins to bind. Collectively, these changes lead to a reprogramming of the LD proteome, as some proteins are displaced while others are newly recruited, ultimately altering cellular and metabolic pathways (19, 28).

Herein, we combine a suite of computational approaches to address several key questions regarding the association of MLX with LDs. We begin by examining how MLX might bind to LDs by analyzing the bound ensembles of probable MLX targeting sequences to TG-rich LDs. We find that the DCD takes on nearly identical conformations in the LD monolayer and the dimer interface. Specific conserved residues are shown to play a central role in this bimodal association. Next, we characterize the dynamics of unbiased association and quantify the relative affinity from biased simulations between TG-rich and SE-rich LDs. This comparison allows us to verify whether the simulations replicate the experimentally observed specificity for TG-rich LD association, shedding light on the mechanisms behind this selectivity. We examine the full mechanism of association for the hairpin, exploring the roles of sequence-specific residues during the association and dissociation processes. We aim to better understand features that distinguish CYToLD proteins beyond their common affinity for packing defects, enabling population-specific and sometimes membrane-specific targeting. Lastly, we examine the implications of protein binding to the LD monolayer, exploring how kinetics and monolayer properties may influence competition between LD proteins.

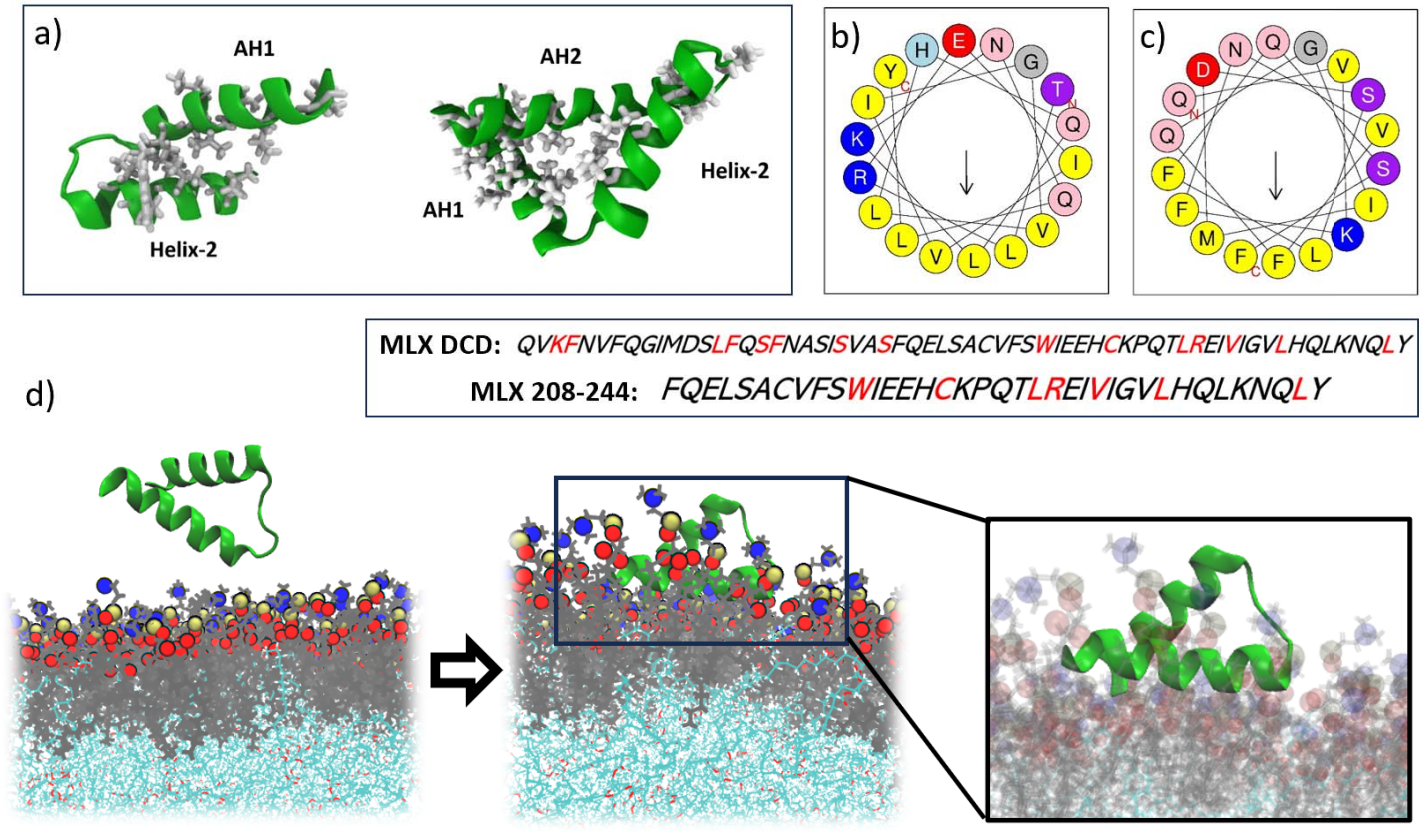

Figure 2. a) Predicted structures of MLX-hairpin (208-244) (left) and MLX-DCD (177-244) (right). b) Both sequences have a conserved AH that contains multiple Leu, Val, and Ile residues. c) MLX-DCD has a second AH with several Phe residues. d) Simulation structures of the initial cytosolic (left, water not shown for clarity) and LD-bound (right) MLX-hairpin.

Methods

The association mechanisms of two MLX sequences were studied: the MLX-hairpin including residues 208-244 (Figure 2 a-left) and the DCD including residues 177-244 (Figure 2 a-right) (for protein structure prediction, please refer to *Supplementary Methods*). MLX-hairpin contains two short helices, one a distinct AH (Figure 2 b), with multiple conserved residues: Leu228, Arg229, Val232, Leu236, and Leu243. Several other hydrophobic residues accompany these; Ile231, Val235, and Leu239. MLX-hairpin was initially thought to be the shortest binding sequence. However, subsequent experiments revealed that it seemed to bind to a variety of membranes, such as the ER bilayer, which means it lacks the specific binding to LDs (R. Farese and T. Walther, personal communications, 2022). Prior work demonstrated MLX-DCD binds specifically to TG-rich LDs (6). MLX-DCD has two AHs (Figure 2 b-c), separated by a middle helix (helix-2) (Figure 2 a-right).

Unbiased MD to capture real dynamics of association for the MLX-hairpin

To explore the dynamics of membrane association, we first conducted long-timescale simulations of MLX-hairpin interacting with 3 LDs, each with a different neutral lipid composition: pure TG, 50:50 SE:TG, and 90:10 SE:TG. The representative LDs were previously equilibrated in long-timescale simulations from our previous work (18, 20) using the CHARMM36m forcefield (29, 30). Previous work has highlighted limitations in the CHARMM36-standard forcefield for TG, as the glycerol backbone is overly hydrophilic in the LD core, leading to an underestimated surface tension at the water-TG interface and overhydration of the LD core relative to the hydration of bulk olive oil (31, 32). Alternative models, such as CHARMM36-cutoff and CHARMM36/LJPME-r, address these issues by reducing the charges to a much more hydrophobic glycerol group until the experimental water-TG interfacial tension is matched. However, these changes also prevent SURF-TGs from migrating into the LD monolayer and hence fail to capture the experimentally measured monolayer expansion of ~15% relative to a bilayer of the same composition (24, 26, 33). This discrepancy has

raised concerns about both the occurrence of SURF-TGs and the overall validity of the CHARMM36-standard model. However, recent work using the Drude2023 lipid forcefield for TG demonstrated that enabling a dynamic charge distribution that responds to polar interface and hydrophobic LD core environments recapitulates all experimental observables, with naturally occurring SURF-TG levels and LD packing defects closely resembling those produced by CHARMM36-standard and quite different from CHARMM36-cutoff (34). Since MLX interacts with the LD monolayer, we opted to continue with the CHARMM36-standard model to ensure proper representation of the interfacial region, featuring SURF-TGs and Drude-consistent packing defects. It should be noted that for proteins deeply embedded within the LD core, it is not yet clear how TG polarization influences protein interactions. The LDs were built using trilayer models, which remain essential for computational efficiency at the all-atom resolution. In these trilayers, a neutral lipid core is inserted between the two leaflets of a phospholipid bilayer. The bilayers were created with the CHARMM-GUI membrane builder (35–37) containing an ER-like composition of 88:37:10 zwitterionic phospholipids: 3-palmitoyl-2-oleoyl-D-glycero-1-phosphatidylcholine (POPC), 2,3-dioleoyl-D-glycero-1- phosphatidylethanolamine (DOPE), and phosphatidylinositol (SAPI), respectively (38–40). Neutral lipid cores with varying ratios of SE:TG (pure-TG, 50:50 SE:TG, 90:10 SE:TG) were created and equilibrated for 500 ns at 310 K in the NPT ensemble using periodic boundary conditions to converge bulk-like properties. The bilayer was equilibrated for 10 ns before separating the leaflets to create monolayers between which the equilibrated neutral lipid box was inserted. The simulation boxes were solvated with 50 Å of a TIP3P water model (41) and 0.15 M NaCl solution on either side of the leaflets. The final systems were then simulated for 8 µs using GROMACS version 2019.4 (42) with a 2 fs timestep. An energy minimization of steepest-decent over 5000 steps was used to get rid of bad contacts of TG and the monolayer leaflets. The temperatures were set to 310 K (physiological temperature) using the Nose-Hoover (43, 44) thermostat and temperature coupling time constant of 1 ps. The particle mesh Ewald (PME) algorithm (45) was used to calculate the long-range electrostatic interactions with a cutoff of 1.0 nm. Lennard–Jones pair interactions were cutoff at 12 Å with a force-switching function between 8 and 12 Å, and pressure was maintained semi-isotropically using the Parrinello-Rahman barostat (46). The pressure was set to 1.0 bar, with a compressibility of 4.5×10^{-5} bar^{-1}, and a coupling constant of 5.0 ps. The hydrogen bonds were constrained with the LINCS algorithm (47). Trajectories were extracted every 100 ps. For a more detailed description of these simulation set-ups, please visit our previous work (18, 20). In this work, the MLX sequences were placed at least 1 nm above the LD monolayer. An energy minimization of steepest-decent over 5000 steps was used to get rid of bad contacts between protein and water, followed by equilibration (noting the LD systems were already equilibrated from the previous studies). Production runs were conducted for a minimum of 1 µs. 15 replicas were run for all systems. Visualizations of the molecular systems were rendered with Visual Molecular Dynamics (VMD) (48).

Association Ensemble Analyses

Contact analysis

To describe the binding process, we used MDAnalysis scripting to measure the center-of-mass (COM) depth of its residue sidechains relative to the phospholipid headgroups' phosphorus atoms, providing a detailed view of the interactions between hydrophobic and polar residues and the lipid bilayer. This was complemented by counting contacts (atoms within 3 Å) between phospholipid and TG defects and residue sidechains, enriching our understanding of molecular interactions. Furthermore, we calculated Radial Distribution Functions (RDFs) to quantitatively analyze dominant interactions within the ensembles, using the MDAnalysis Python library (49).

Defect size below protein

To determine the size of the packing defects involved below the proteins, we calculated the convex hull area of the protein residue interactions with the defect pockets. Calculating the convex hull below the cutoff of the P atoms of the PLs allows us to determine the size, and depth of defects directly below the protein. The convex hull of a group of points S in n-dimensional space can be thought of as the smallest convex shape that encompasses all points within S. For N points $p_1,\ldots,p_N$, the convex hull C is then given the expression:

$$C \equiv \left\{ \sum_{j=1}^{N} \lambda_j p_j : \lambda_j \geq 0 \; for \; all \; j \; and \; \sum_{j=1}^{N} \lambda_j = 1 \right\}$$

Where p is a combination of 10 sidechains below the defect cutoff (50). If there was an inadequate number of sidechains below the cutoff, the convex hull was not counted (50). The size of the convex hull was averaged over the respective trajectory of 1000 frames. The MDAnalysis Python library was used for the scripting.

Packing defect analysis

We refined a Cartesian-based algorithm to quantify lipid packing defects within monolayer leaflets, building upon established methodologies (20, 51–53). Put briefly: For a monolayer leaflet, the lipid atoms whose positions were greater than the threshold (Z_{thr}) were projected onto a 1 Å spacing two-dimensional (x–y) grid. The threshold (Z_{thr}) was set to the average z-position of the phosphorous atoms of the leaflet minus 2 nm, which therefore encompasses most atoms of the respective leaflet. We first defined the van der Waals radii for a comprehensive set of atom types taken from the CHARMM36m (30) parameter set. This informed our overlap criteria between grid points and atoms, ensuring accurate defect localization. If a grid point overlaps with an atom (center of atom and grid point is less than atom's radius plus half of the diagonal grid, ($\sqrt{3/2}$Å), the z-position of the atom and the atom type are saved in the grid point. If the grid point overlaps with a polar PL headgroup, then it is not considered a defect. While scanning the grid using a depth-first search, if the grid point overlaps with PL-acyl groups or the LD-neutral lipids, then it is considered a defect. For each of these defect types, the neighboring elementary defects are clustered into one. If the clustered defect contains N elementary defects, it is considered to have a defect size of N Å^2.

The probability of finding a defect with size N was computed and fit to an exponential decay function:

$$P(N) = ce^{-N/\pi},$$

where c is the normalization constant and π is the packing defect constant. The packing defect constant represents how slowly the decay function falls off. A higher packing defect constant would generally mean that there is a higher probability of finding a larger defect. The original script for this packing defect analysis can be found at (https://github.com/ksy141/SMDAnalysis).

We additionally modified the code to create cut-offs that excluded a desired radius from the protein once the protein associated to the respective leaflet of the LD monolayer. This allowed us to identify the alteration of monolayer defects due to protein interactions. To track the protein-defect interactions over time, we included further analysis to include the protein, while isolating specific heavy-atom interactions that were below defect threshold cut-offs. These protein atoms were included in the defect analysis and depth-first grid search, but were not included as a defect type. If a heavy protein atom crossed the threshold of the defect in the x-y grid, it was counted as a defect-protein interaction. Modified packing defect script analysis scripts that account for protein cutoff distances, and identifications of top and bottom leaflets can be found at (https://github.com/jaybraunjr/PD). Error bars for packing defect constants were calculated using blocking averaging, with 10 blocks used over a 500 ns period.

Coordination analysis

The coordination of specific residues to the defects is determined by:

$$s = \sum \left[1 - \left(\frac{r_i}{r_0}\right)^6\right] / \left[1 - \left(\frac{r_i}{r_0}\right)^{12}\right],$$

where r_0 =0.4 nm, and r_1 is the distance between the side chain group and defect group. Heavy atoms were used.

Tail Order Parameters

The tail order parameters are calculated with:

$$S = \langle \frac{3}{2} \cos^2(\theta - 1/2) \rangle,$$

with θ being the angle between the position vector of a carbon atom of an acyl chain bonded to a hydrogen with respect to the system normal. A larger value of S Indicates increased ordering in the membrane. The brackets represent the ensemble average (54). The tail order parameters were calculated with MDAnalysis scripting.

Mean squared displacement

To analyze the mobility of lipids in our system, we calculated the mean-squared-displacement (MSD) of lipid molecules over time. Lipids were tracked over the course of the simulation, and their positions at each time interval were recorded. The MSD was then computed using the Einstein formula through MDAnalysis (49, 55, 56).

$$MSD(\tau) = \langle \frac{1}{N} \sum_{i=1}^{N} |r_d - r_d(t_0)|^2 \rangle_{t_0},$$

where τ is the time lag, and $r(t)$ is the position of the lipid molecule at time (t). By plotting the MSD against the time τ we were able to derive a linear relationship for the diffusive regime. The lipid diffusion coefficient D was then determined from the slope of the MSD curve, using the relation: $MSD = 4D\tau$ for a two-dimensional system. This provided us with a quantitative measure of how rapidly lipids were diffusing through the monolayer, allowing for a deeper understanding of the lipid dynamics within our system.

Binding of MLX-DCD domain

After conducting three 1-µs unbiased simulations, it was found that the MLX-DCD system couldn't bind to the LD monolayer. This was due to the tendency of the three helices to fold upon each other in order to prevent the hydrophobic residues from interacting with the cytosol. Without very long-timescale simulations, it is unlikely to attain binding. A slight bias using steered MD (57) was used to open the AH1 and AH2 of the DCD to expose them to solution, and then steered MD was also used to slightly bias the COM of the protein towards the LD in the z-coordinate until initial contact with the membrane surface was observed. A bias of 1000 kJ, with a rate of 0.001 nm per ps was used. Following this initial contact, regular production MD parameters were used as previously described. The simulation was run for an additional 3 µs, and the stability was measured using root mean squared deviation (RMSD). Additionally, we created a larger MLX DCD system (DCD-big) by doubling the x and y dimensions to $20\ nm \times 20\ nm$. This was done to account for any size or pressure artifacts that might appear due to the large protein with reference to the LD monolayer (58, 59).

Quantifying association affinity

Umbrella sampling (US) (60) was used to determine the free energy of association for both the MLX-hairpin and MLX-DCD segments. The potential of mean force (PMF) was calculated as a function of the z-coordinate of the COM of the respective peptide sequence with respect to the distance from the average PL phosphorous z-coordinate plane. For MLX-hairpin, 22 windows were used, and for the MLX-DCD, 20 windows were used, with 0.125 nm used as the window spacing (histogram overlap available in Figure S2). The windows were obtained through natural binding in the pure-TG and 50:50 SE:TG systems, and through partial association event in the 90:10 SE:TG and the DCD. Steered MD, as described in the previous section, was used to fully associate the proteins in which partial association occurred. A harmonic potential with a force constant of 1000 kJ/mol nm^{-2} was used as a distance constraint. There was no helical restraint, as the helices remained extraordinarily stable throughout the simulations. The rest of the simulation parameters were the same as described in the unbiased simulations mentioned previously. Simulations were run for a total of 110 ns with the first 70ns being used to equilibrate the systems until the fluctuations were noticeably converged. The Weighted Histogram Analysis Method (WHAM), specifically using the tool g_wham (61), was used to generate PMF, with error bars being generated from block averaging using four 10 ns chunks of the last 40 ns. Simulations were run using GROMACS version 2019.4 (42).

Results

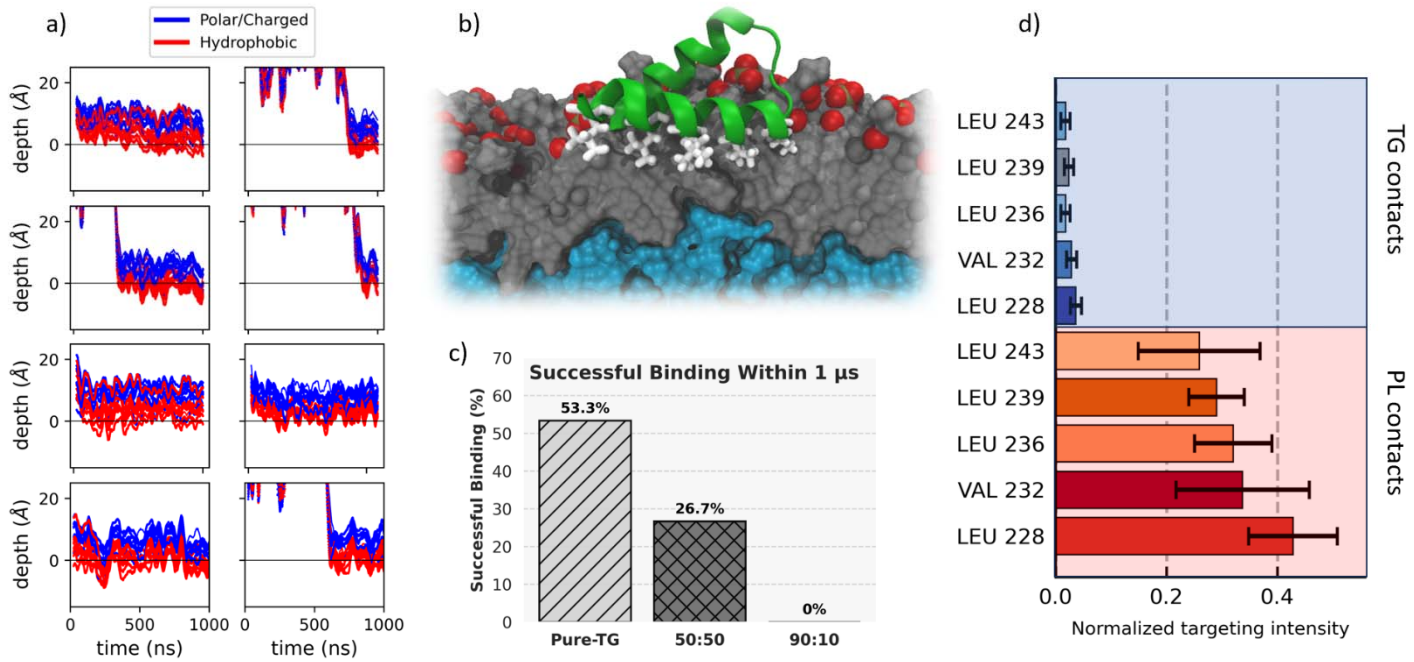

Figure 3. MLX binds to TG-rich LDs using its hydrophobic face. a) The red lines represent hydrophobic residues while the blue lines represent charged or polar residues. The black line at 0 represents the average location of the phosphorus of the PL monolayer. In all association cases, the hydrophobic residues are facing towards the membrane, meaning it is the hydrophobic face that is responsible for binding to defects. b) MLX buries its conserved hydrophobic residues of the AH into monolayer packing defects. c) The success rate at which protein-LD binding occurs for the differing systems. d) Normalized targeting analysis reveals contact analysis trends of all 8 bound replicas.

MLX targets TG-rich LDs through sequence-specific hydrophobic and charged interactions

LD association of the MLX-hairpin was first explored through parallel, long-timescale, unbiased simulations starting with the hairpin ~2 nm above the monolayer leaflet, as if in the cytosol (Figure 2 d). Although observed properties are not expected to be statistically converged, unbiased simulations are essential for exploring the association mechanism with real dynamics unaltered by a Hamiltonian bias. Focusing first on AH1 (residues 228-244), the MLX-hairpin was considered fully associated once the center-of-mass (COM) of 4 or more hydrophobic residues transitioned from the cytosol to positions at or below the plane defined by PL phosphorous atoms (solid lines at y=0 in Figure 3 a) and stabilized there. Such complete immersion occurred within 1 µs in eight out of fifteen instances in a pure TG environment, and four out of fifteen instances in the 50:50 TG:SE LD. No such association was observed in the fifteen 90:10 SE-rich LD simulations (Figure 3 c). Tracking the dominance of specific residue-monolayer interactions via contact analysis (Figures 3 a and d, and S3), Leu228 had the most interactions, closely followed by Val232 and the trio of leucines (Leu236, Leu239, and Leu243). This was confirmed by the normalized targeting intensities that determine the preference of residue-defect interaction (Figure 3 d). Interestingly, these hydrophobic interactions predominantly occurred with PL acyl chains, rather than TG molecules (Figure 3 b and d).

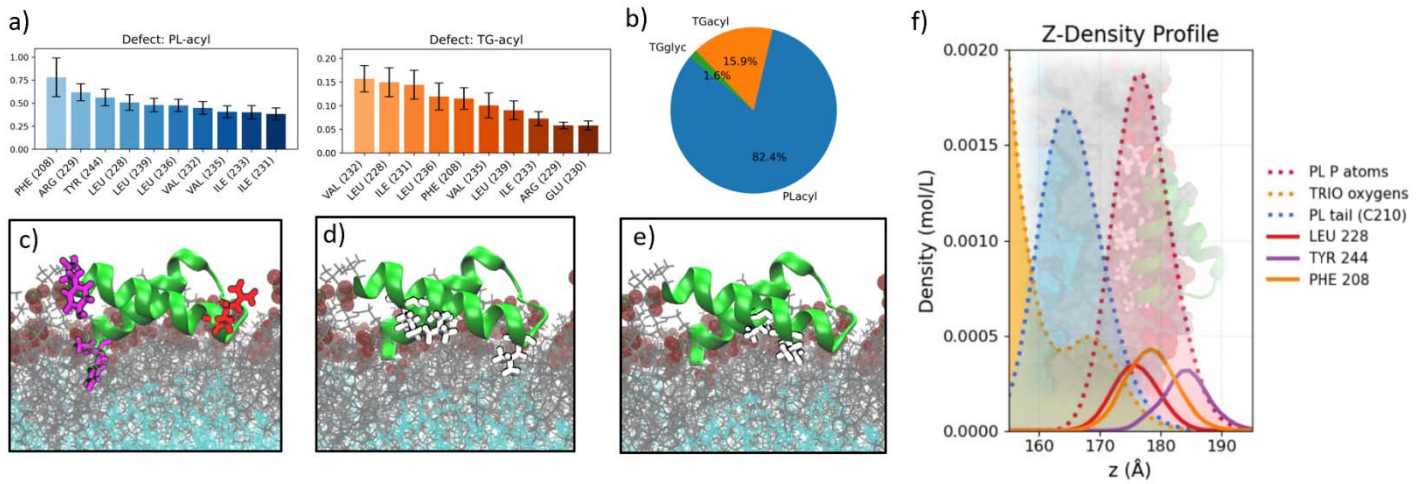

Figure 4. Defect analysis reveals the preferred interactions. a) Normalized total defect interactions of both the PL-acyl and TG-acyl induced defects (Error bars taken from SEM of all trajectories in which binding occurred). b) PL-acyl defects are the dominant defect types. c) Tyr, Phe (purple), and Arg (Red), are the dominant interacting residues. d) A series of leucines and e) valines are also critical for defect interactions. f) The depth of the residues are relatively shallow, right under the PL phosphorus's (red), and interacting with the upper PL tail (blue).

To further refine the role of packing defects in MLX association, residue interactions within a specified cutoff of membrane defects (see Methods) (Movie 1,2) were quantified. Residues Arg229, Phe208, and Tyr244 act as anchoring residues, maintaining the most significant interactions with defects (Figure 4 a and c). A series of leucines (Figure 4 a, d), valines (Figure 4 a, e), and isoleucines, many of which are conserved, exhibited strong coordination with packing defects. Consistent with the contact analysis, these residues preferentially interacted with PL acyl chains, followed by TG acyl chains, and showed minimal association with TG glycerol headgroups (Figure 4b). This preference is further supported by the z-dimensional density analysis, which shows that LEU 228, TYR 244, and PHE 208 remain relatively shallow when embedded in defects (Figure 4 f). Rather than penetrating deeply into TG-rich regions, these residues tend to orient toward the PL headgroup region and interact with the upper segments of PL acyl chains. Additionally, we looked at residues that might coordinate with PL-headgroups. Lys240, which is on the polar side of the AH, also acts as a stabilizing residue through electrostatic interactions with the PL headgroups (Figure S4 a-c). Arg 229 creates similar interactions with the guanidinium group interacting with PL-headgroups, while the rest of the hydrocarbon chain is sucked into a defect shared by Leu228 (Figures 4 c, S4 a-b and d).

MLX-DCD binding involves exchange of hydrophobic interactions

The MAX- and MYC-network of proteins share a common basic helix-loop-helix leucine zipper fold (Figure 1, S1). Recent NMR work has shown that even the basic region, commonly thought of as disordered, retains some degree of helicity (62). Thus, the Alphafold predicted structures of the MLX monomer (Figure S1) and homodimer (Figure 1) were all reported with a high degree of confidence (pLDDT scores above 90). The MLX DCD, positioned above the C-terminal domain of the leucine-zipper, is nearly identical between the dimer and monomer, forming a triangular planar structure with the AH1 and AH2 overlapping slightly to trade hydrophobic interactions (Figures 1 and S1 b). Additionally, the AlphaFold predicted heterodimer with MondoA shows a similar structure, with the MLX-DCD forming a planar interface with the MondaA-DCD, maximizing the AH1 and AH2 interactions at the dimer interface (Figure 1 b). In the cellular environment, the MLX distribution between monomer, dimers, and LD-bound pools likely involves a dynamic exchange of the DCD between dimer interfaces and LD monolayer. However, during simulations of the DCD monomer alone, the absence of a dimer interface or the rest of the MLX monomer results in the DCD helices folding in slightly, as captured in Figure 2a-right, to minimize exposure of the hydrophobic residues to water. This conformation is reasonably stable with minimal fluctuations. When placed above the TG-rich LD no stable binding events occurred within 1 µs in 3 replicas, which is expected given even a modest kinetic barrier for the buried hydrophobic residues to open and interact with the

monolayer. To overcome this kinetic barrier, a slight bias was applied to open the DCD conformation and expose the hydrophobic AHs to the cytosol, enabling monolayer association (see Methods). Once bound, all three DCD helices form extensive interactions with the membrane (Figure 5, Figure S5 a-c), with the two AHs burying into the PL-acyl defects. Consistent with the bound pose of the MLX-hairpin, AH1 (Figure 5a-b, and S6) makes abundant interactions with the PL-acyl defects, while AH2 has several phenylalanine's that also embed into PL-acyl defects (Figure S5 c). The catch and anchor residues also play a similar role (Figures 5 a and S6) as they did with MLX-hairpin

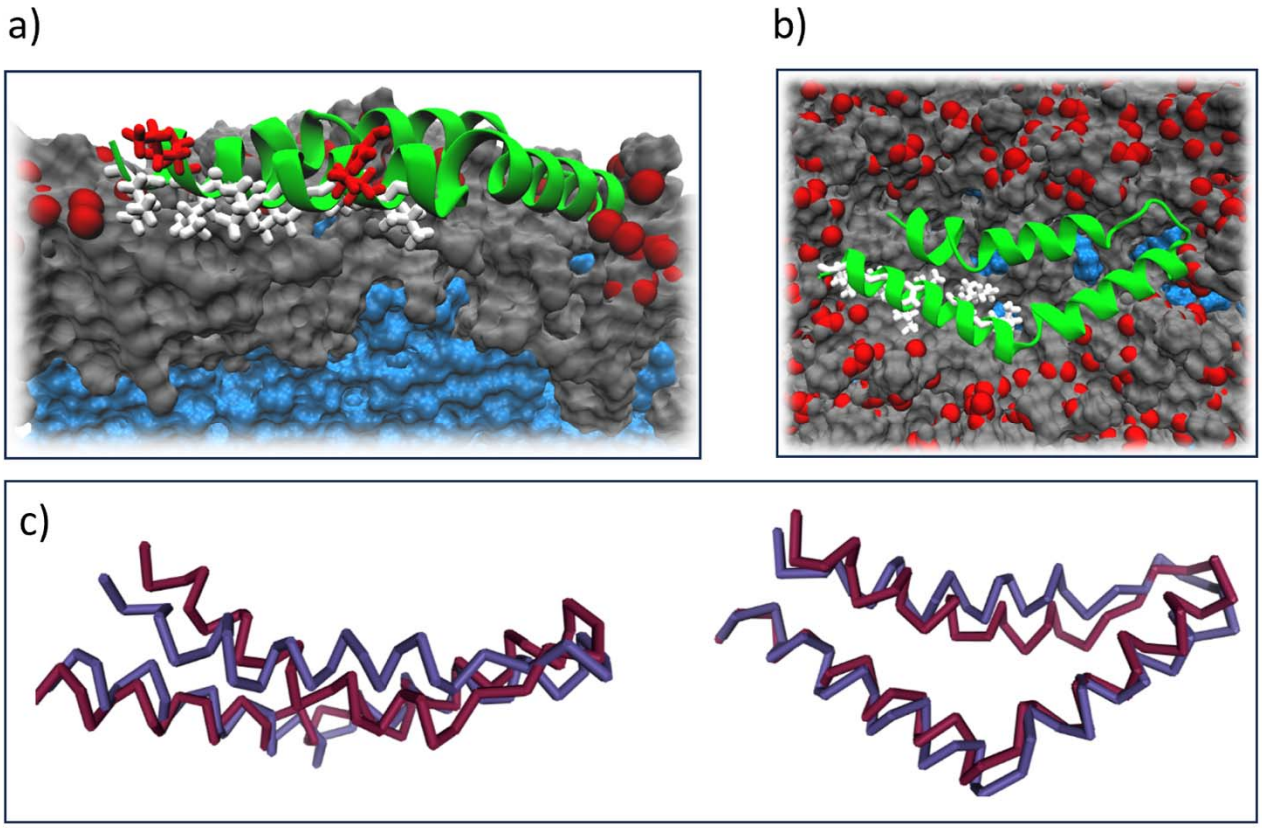

Figure 5. a) The DCD uses the same AH residues (colored in white) to bury into PL-acyl defects. The red residues are the Arg and Lys interacting with PL headgroups. b) Top-down view of the DCD embedded into the PL-acyl defects. The structure is almost identical to its dimerized form. c) Nearly perfect overlap of one of the DCD homo-dimer chains (red) to the final LD-bound structure (blue).

Unexpectedly, the LD-bound DCD structure is nearly identical to the DCD-dimer structure, suggesting the burial of hydrophobic groups in the dimer mimics that in the LD membrane (Figure 5 b and c). The conformation is very stable once bound, as demonstrated by the backbone RMSD (Figure S7). As expected, DCD binding induces larger defects than those typically present on an LD over long timescales. The size of the defect tracks the size of the associating helices. Over an average of 1000 frames, the size of packing defect directly below the MLX-DCD domain is , while that under the MLX-hairpin is (Figure S8). Thus, the larger MLX-DCD domain both requires and induces a larger defect, displacing more PL headgroups. This likely explains targeting specificity to TG-LDs since they have larger and more frequent packing defects than bilayers (18, 20).

Thermodynamics of association supports preferential targeting to TG-rich LDs

To confirm that the insights found in unbiased simulations are reflective of ensemble behavior, association free energy profiles with varying LD compositions (pure-TG, 50:50, and 90:10 CHYO:TG ratios) were computed (Figure 6 a and b). These profiles show a clear preference for MLX-hairpin binding to the 50:50 and pure-TG LDs, with a pronounced

association affinity of ~11-12 kcal/mol. Conversely, the 90:10 LD system presented an energetically unfavorable profile for monolayer interaction, favoring MLX's cytosolic location by 4 kcal/mol. The MLX-DCD domain exhibits a discernible ~19 kcal/mol binding affinity for the TG-LD monolayer. In contrast, when interacting with the 90:10 LD monolayer, it raises the free energy by ~15 kcal/mol, effectively repelling it (Figure 6b). These findings are congruent with the hypothesis that packing defects and monolayer density critically influence protein-LD affinity.

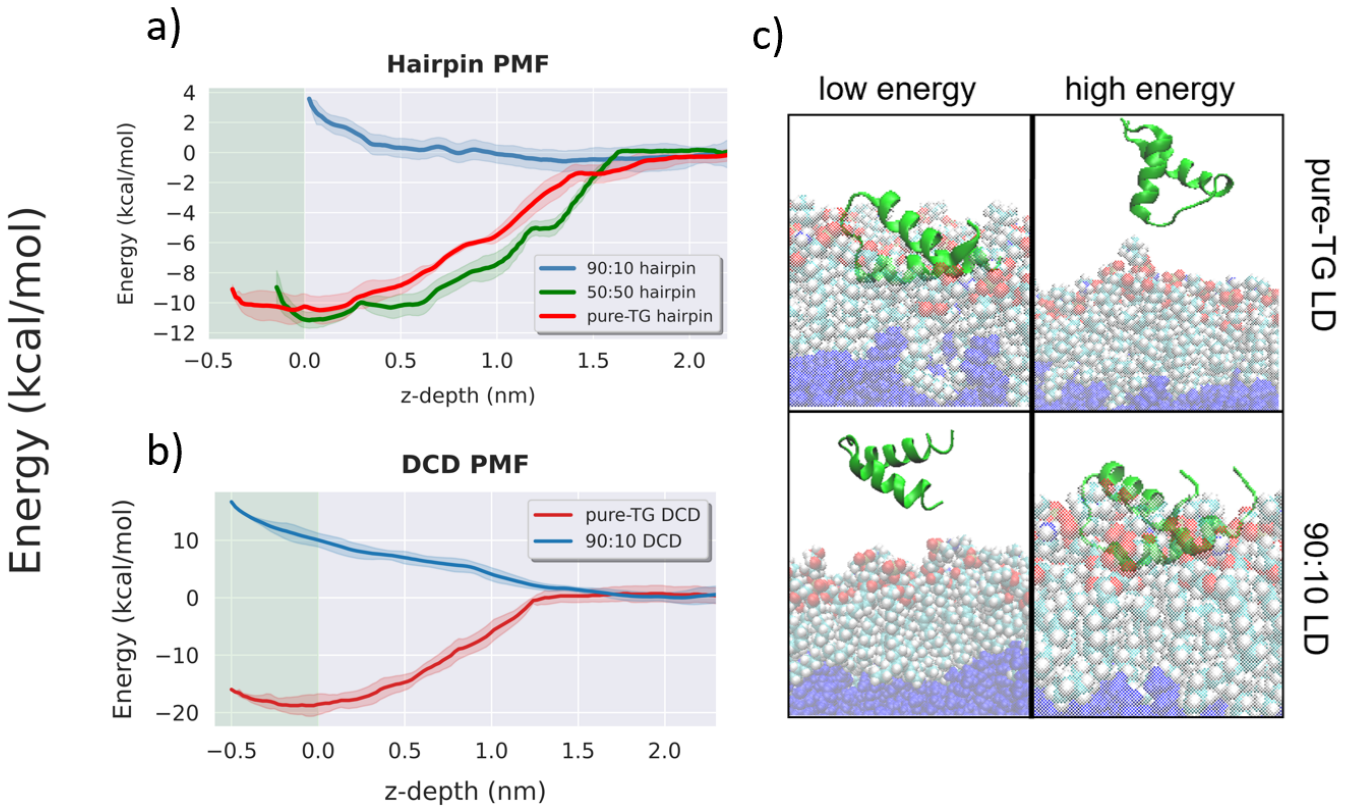

Figure 6. a) Free energy profiles for LD association and dominant stable (low energy) and unstable (high energy) conformations show that MLX has a strong affinity for the TG and 50:50 SE:TG LDs, but is repelled from the 90:10 SE:TG LD. The sampled reaction coordinate (x-axis) is the z-COM distance of MLX from the phosphate plane (x = 0) of the LD monolayers. The green shaded area from -0.5 to 0.0 represents the PL-monolayer, while x > 0.0 moves into water. Error bars were calculated using block averaging (see Methods).

Focusing on the bound conformations from the biased simulations (z = 0 in Figure 6a), the MLX-hairpin shows consistent contacts between charged residues (Arg229, Lys240) and the PL headgroups in both the TG-rich and 90:10 CHYO:TG LD systems (Figure S9). In contrast, conserved hydrophobic residues engaged with the inner acyl chains (C2, C3, C4) in pure-TG LDs, but not in the 90:10 system. Thus, MLX attempts to bind to the 90:10 CHYO:TG, engaging in headgroup interactions, but fails due to the inaccessibility of the PL tail region for hydrophobic residues (Movie 3).

Heterogeneous association pathways share catch-anchor-embed mechanism

Time-resolved defect analysis reveals that association occurs through multiple interaction pathways (Figure S10), although each converges to the same bound pose (discussed below). Several key 'catch' residues emerge as initiating and anchoring monolayer association. Arg229, located at the hairpin kink (Figure 7 a), initiates association in 5 out of 6 tracked binding events (Figure S10 a, b, c, e, f). This is expected given arginine's strong electrostatic attraction to PL phosphates (Figure 7 a, Figure S4 a-d), while additionally being placed next to the conserved Leu228, which buries deep

into defects. In 3 out of these 5 events (Figure S4 a, b, f), Tyr244, which is at the other end of the AH (Figure 4 a, and 7 a), soon thereafter forms a hydrogen bond with PL headgroups (Figure 7 a) though in time it sinks below the headgroups to satisfy dispersion attraction to PL-acyl defects. Anchoring both sides of the AH with Arg229 and Tyr244 can happen concomitantly with helix 1 association (Figure S10 a), or it can anchor the AH in the headgroup region via polar interactions until a defect sufficient for hydrophobic burial forms (Figures S10 b, f, and 7 b). In other cases, submersion happens from the kink initiated with a SURF-TG (Figure S10 c) or via rapid hydrophobic burial (Figure S4 e). In one case, Phe208, which is on the other side of helix 1 and often is involved in early helix-2 association, acts at the initial catch residue (Figures S10 d, and 7 a). Thus, although these binding pathways vary between replicas, the strategic placement of catch residues at the ends of helices enhances monolayer association. Additionally, anchoring the protein close to the membrane provides time for the hydrophobic groups to transiently 'snorkel' above (Figure 7 b) before fully embedding into defects (Figure 7 c).

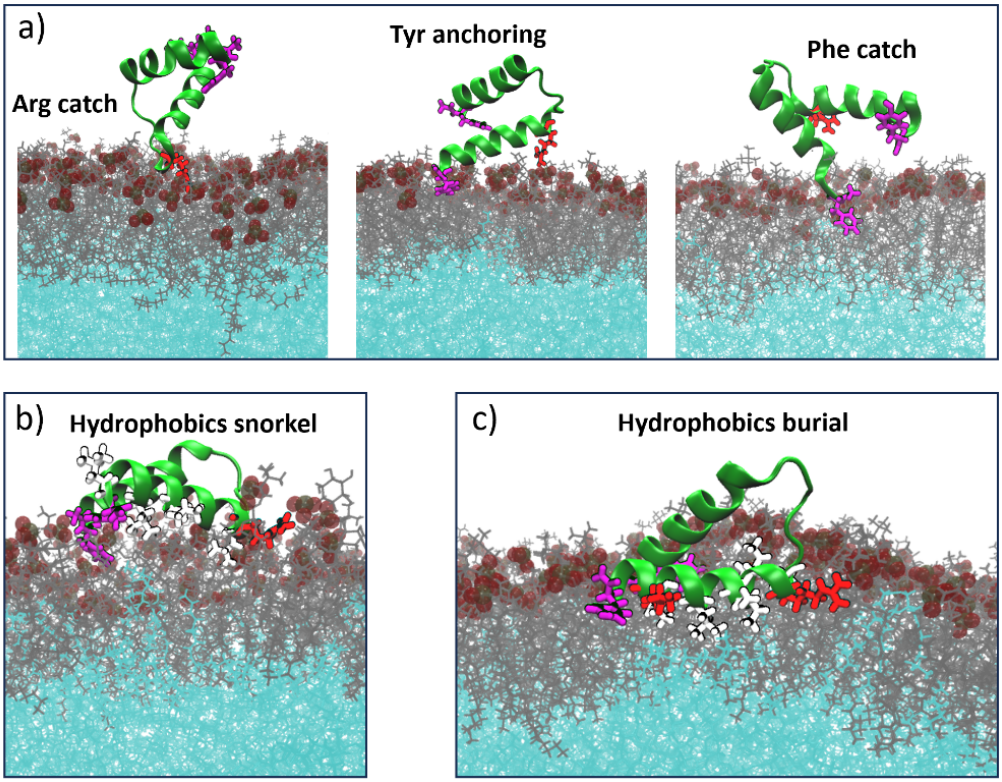

Figure 7. a) The catch residues are Arg, Tyr, and Phe on the termini and kink of the protein. b) After the initial catch, the hydrophobic residues snorkel on the surface, trying to embed into a defect. c) Finally, the hydrophobic residues find and create an adequate defect, burying the AH deep into the PL-acyl tail region (Lys240 also pictured in red on left side of AH, as it assists with coordination to PL headgroups).

MLX changes conformation upon association to form stabilizing interhelical interactions.

In addition to the stabilizing interactions with the LD monolayer, both the MLX-hairpin and MLX-DCD engage in interhelical interactions once bound. This is particularly pronounced for the MLX-hairpin.

Although both AH1 and helix-2 remain independently folded throughout the simulations, there is a clear inter-helical conformational change upon association with the LD monolayer. In the cytosol, the two helices are flexible, occasionally engaging in hydrophobic interactions but largely fluctuating in relative tilt angles (Figure S11 a). However, they transition to a conserved 'crossed' configuration upon membrane association (Figure 8 b-4 and d) with the AH1 tilting upwards (~5 degrees) while helix 2 tilts downwards (-35 degrees) (Figures 8 d and S11 a). To demonstrate the convergence toward a conserved bound conformation, we projected the free energy landscape of the simulations onto RMSD vs. COM distance to monolayer and protein end-to-end distance vs. COM distance to monolayer (Figures 8a–b). In both plots, the bound state is characterized by low RMSD, low COM distance, and a conserved end-to-end distance. This consistent clustering highlights a well-defined and reproducible bound pose adopted across simulations. Additionally, association can be determined only by observing RMSD vs. protein end-to-end distance free energy projection as well (Figure S11 b). The final bound conformation exhibits notable stability, as confirmed by the alignment of the last bound structure frame across 8 simulation replicas (Figure 8 e). This stability arises from a network of inter-helical interactions, including hydrophobic contacts and hydrogen bonds (Figures 8 f, and S12 a-d), enabled by complementary interactions with the LD monolayer. Notably, the number of hydrogen bonds between the helices doubles in the bound state (Figure S12 b), with new hydrogen bonds forming between Lys and Glu residues at the sequence's kink region (Figures 8 f, S12 c and d). More specifically, the Lys224 initially makes backbone hydrogen bonds with Gln226. After binding, the sidechain of Lys224 then starts to make h-bonds with the Glu230, while several other polar residues start trading h-bonding interactions as well. Collectively, this network of interhelical interactions stabilizes the bound pose. As previously demonstrated (63), interactions between helices enhances affinity to the membrane indirectly, since the dissociation of one helix requires dislodging the other as well, making it statistically less likely. We anticipate that interhelical interactions play a central role in a strong membrane affinity, both for AH's in general and for the MLX-hairpin specifically. Thus, the binding process is dynamic with multiple specific association pathways as the MLX-hairpin finds its way to a consistent, stable bound conformation (Movie 4).

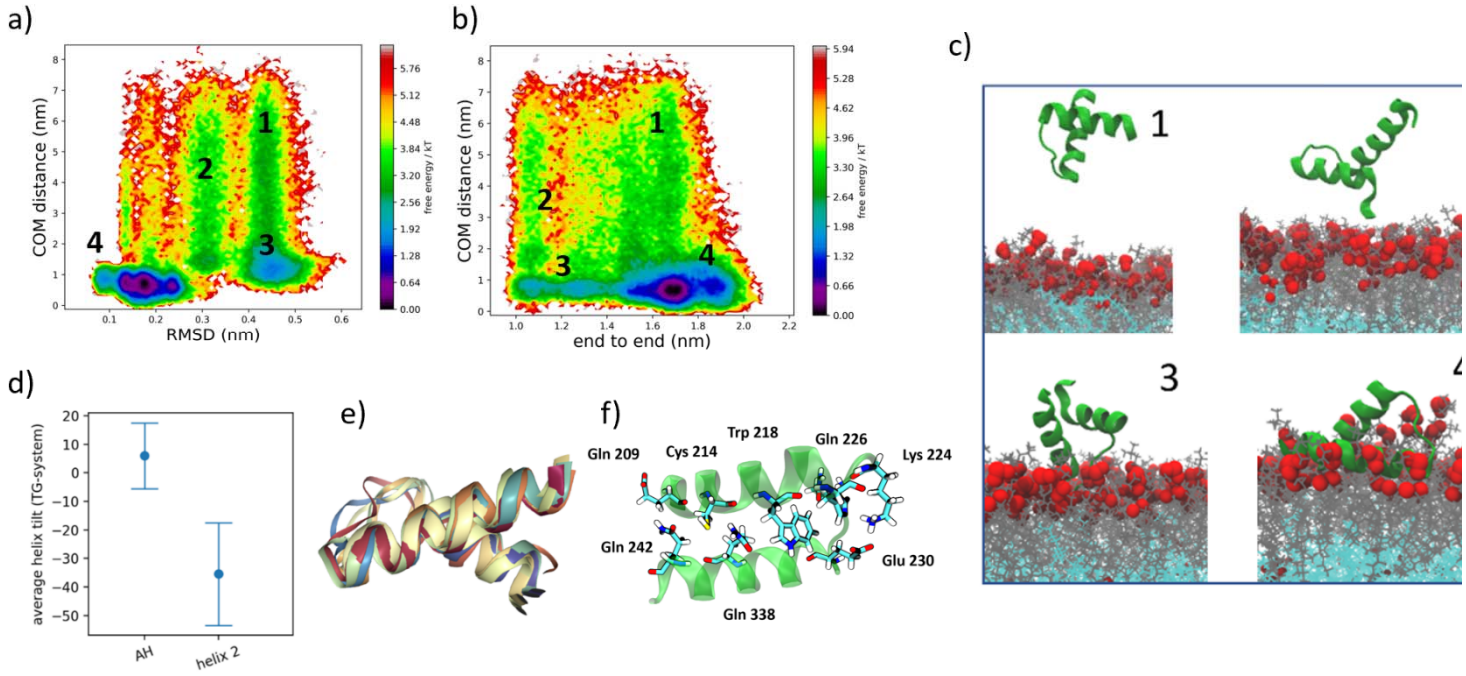

Figure 8. a) RMSD versus center-of-mass (COM) distance reveals multiple metastable wells, with the fourth well representing the most stable bound state. b) A similar trend is observed in the COM versus end-to-end distance plot, further supporting the identification of the stable conformation. c) Representative structures from each metastable well highlight the conformational diversity of the MLX-hairpin, with the fourth structure exhibiting

the most compact and stable binding mode. d) The final bound pose maintains a specific tilt angle between the two helices. e) Overlap of the bound conformation from the 8 trajectories that resulted in binding shows consistency in the final bound conformation, stabilized by f) multiple interhelical interactions.

Association of MLX alters LD monolayer

An unexpected finding in this work was that the association of either the MLX-hairpin or MLX-DCD, as small as they are, seemed to alter the physical properties of the LD monolayer. To quantify this impact, we focused on the monolayer composition, defect organization, PL-tail order parameters, and dynamics. To verify these properties are not artifacts due to the size of the system, we created the DCD-big system with twice as large dimensions, quadrupling the surface area of the LD monolayer.

Defect Composition Alteration: Upon MLX association, we observed a decrease in the probability and size of defects surrounding the protein on the protein-bound leaflet in each system (MLX-hairpin, MLX-DCD, MLX-DCD-big) (Figure 9 and Figure S13). This was quantified by measuring probability and likelihood of defects, specifically focusing on defects more than 1 nm from the protein. Defects are smaller, on average, on the protein bound leaflet as demonstrated by the analysis of defect probability versus size (Figure 9 e) and as can be seen visually in a top-down view of MLX-DCD (Figure 9 f, g). We subsequently quantified the defects by calculating the defect constants. A higher packing defect constant would generally mean that there is a higher probability of finding a larger defect (see Methods for details). All defect types were smaller on the protein-bound leaflet (Figure 9 a-c). As expected, the magnitude of deviations decreases from the MLX-DCD to the MLX-DCD-big system. This is consistent with the impact of the protein being both localized to the region around it and modulated by the size of free membrane.

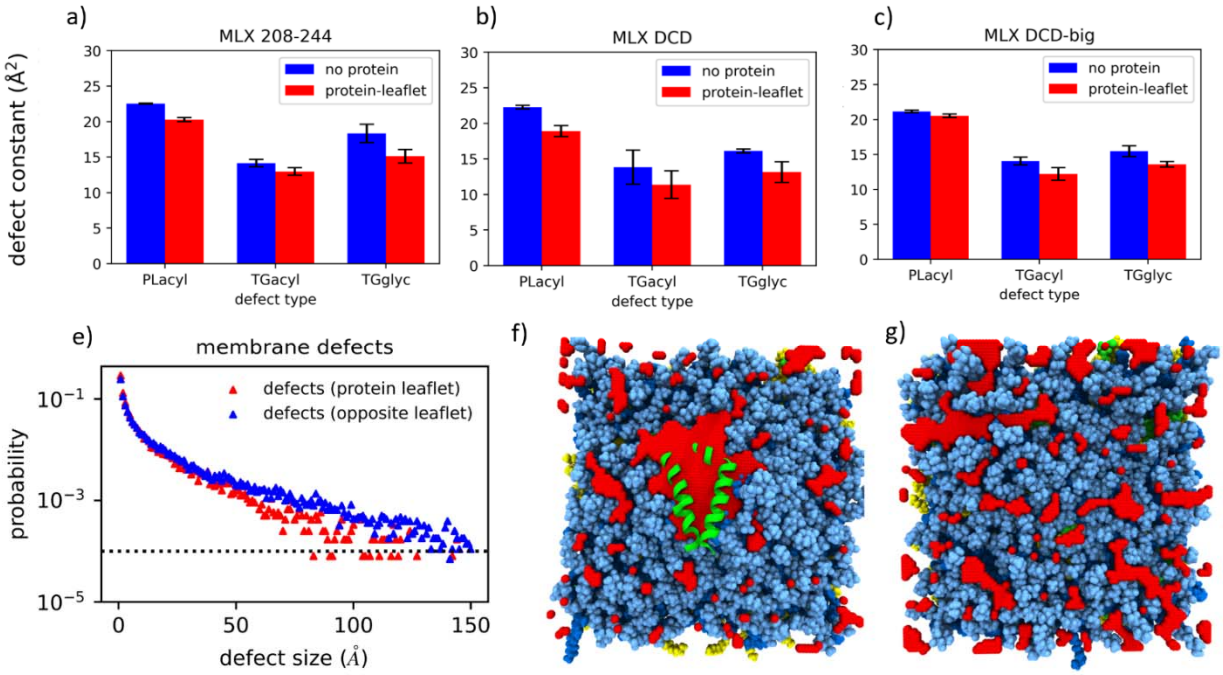

Figure 9. Packing defects of protein-bound leaflets are smaller than those of LD leaflets without association. The packing defect constants for a) the MLX-hairpin, b) MLX DCD, and c) MLX DCD-big all have smaller defects at a cut-off of more than 1 nm from the protein. Error bars were calculated from block averaging (see Methods). e) The probability vs defect size again shows that the defects are smaller on the protein-bound leaflet for MLX DCD. The decrease in size and quantity of defects distal from the protein is apparent from the top-down view comparing the f) DCD-bound leaflet and g) free leaflet. PL-headgroups are blue and defects are red.

SURF-TG Composition: SURF-TGs, commonly found in TG-rich LDs, decrease in number when the MLX sequences are bound, dropping to approximately 1.5% of the monolayer composition (Figure 10 f). The opposite leaflet of the LD system maintained a normal SURF-TG composition (3-6%). The trend was maintained for all the systems. The number of SURF-TG molecules has been clearly correlated with the magnitude of applied surface tension (21, 34). Under an applied surface tension, mimicking an expanding LD with limited PL's to grow the monolayer surface, more TG molecules are brought into the monolayer. This both modulates the magnitude of surface tension and alters the packing defects, giving LDs an expansion-specific property for proteins like CCT to target (21). It seems that the association of an AH-containing protein has the opposite effect, displacing PL headgroups, decreasing surrounding packing defects, and pushing SURF-TG back into the LD core. Thus, association induces a shift in composition that again could influence the association of competing proximal proteins.

Tail-Order Parameters: PL tail-order parameters are indicative of how ordered the PL tails are as a function of position, with C1 being just below the glycerol moiety and C16/C18 being the last carbon in the tail (Figure 10 a-c). As anticipated, the PLs immediately below MLX-DCD were more disordered (Figure S14 b). However, those distal from the protein by more than 2nm exhibited greater order compared to those in leaflets without protein (Figure 9 a-c). This also held true for the MLX DCD-big system (Figure S13 a). Even 1-2nm away the increase in order is apparent. From 2+ to 3+ nm the increase in order is consistent (Figure S13 b). Thus, association of an AH containing protein displaces PL headgroups, decreasing the order in the PL tails immediately around and under it, but also increases the order in the surrounding PLs. This is not immediately obvious. It could be assumed that the increased disorder of the PL tails under the protein would spread such that all PLs within a given cutoff would be more disordered. Thus, a concern was that the observed increase in order is simply an artifact of the system size and the increased packing that protein association would cause in the membrane-bound leaflet. In a real membrane system, this would be alleviated by monolayer expansion. However, these trends were not altered when the system size was doubled (MLX-DCD-big), suggesting it is not purely an artifact of system size. However, these impacts should always be considered in the context of the system. The magnitude of increased packing order in some region surrounding the protein will be influenced by the nature of the surrounding membrane. Packed monolayer membranes with many associated proteins would likely be more impacted while empty monolayers with facile expansion would more quickly dissipate the increased proximal order.

Dynamics and Fluidity Analysis: To analyze the dynamic fluidity of the monolayer the mean square displacement (MSD) of PLs was evaluated in the DCD-big system. We found that the MSD for all PL types was larger in the leaflet without associated proteins (Figure 10 d-e). This was further corroborated by the lateral diffusion coefficients (Table S1), indicating that protein association reduces the fluidity of membrane PLs. These findings collectively demonstrate that the association of MLX-DCD with LDs not only changes the defect composition but also influences the ordering and dynamics of the surrounding membrane.

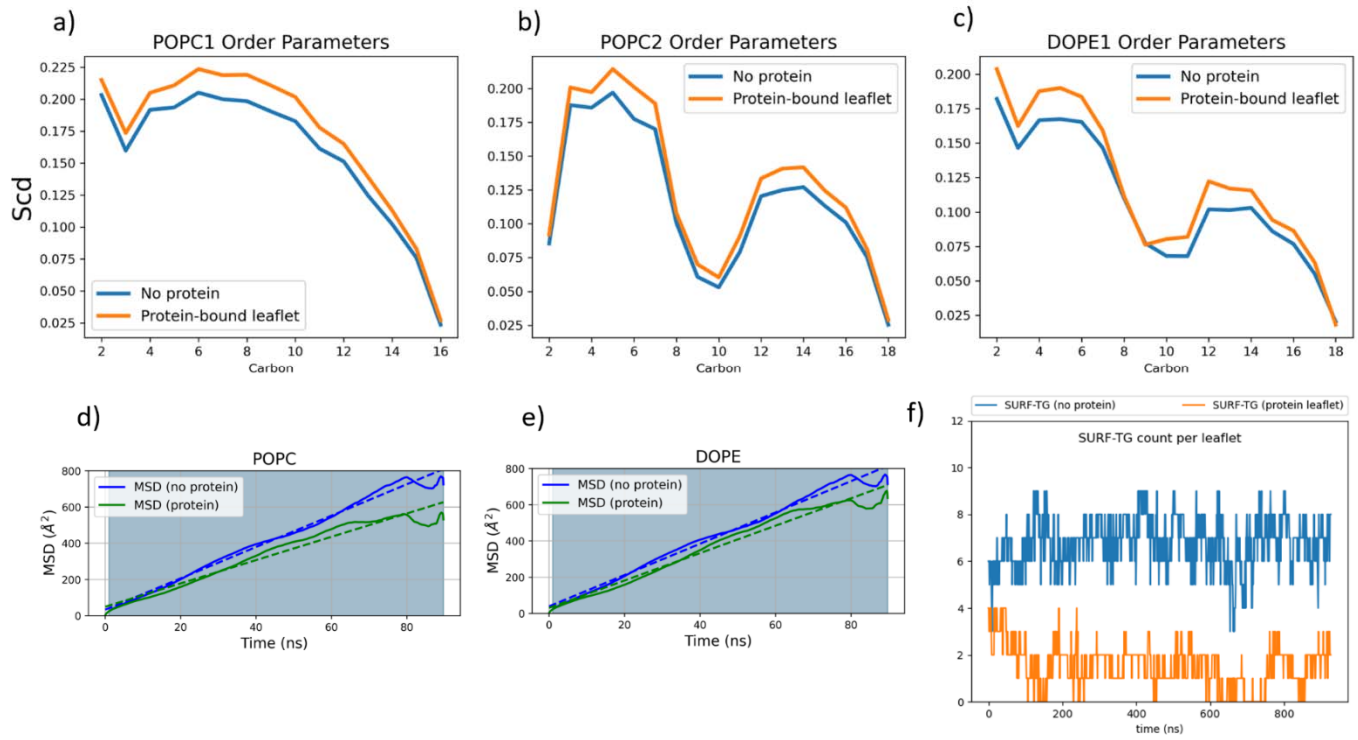

Figure 10. a-c) Tail order parameters for the protein-bound leaflets are elevated compared to those in the free leaflet. d-e) Additionally, the MSD for the protein-bound leaflets decrease in magnitude. f) Due to the changes in the LD monolayer, the number of SURF-TG decreases (data shown for MLX-DCD is representative of other systems).

Discussion:

MLX, a transcription factor in the MAX network, regulates glucose metabolism and energy homeostasis through heterodimer formation with partners like MondoA (7–9), enabling its nuclear translocation and transcriptional activity. However, in the presence of TG-rich LDs, MLX associates with the LD surface, sequestering it in the cytosol and modulating its activity (6). This inactivation of MLX by LD binding is particularly significant within the context of MAX-network transcription factors, such as MYC, which are often dysregulated in cancer and linked to tumor progression (64). Similar to MLX, many other CYtoLD proteins dynamically associate with LDs throughout their lifecycle (2), adapting to shifting metabolic needs (3, 5, 65, 66). Unlike the ER, LDs lack specialized protein-association machinery, such as the translocon. Selective LD association has traditionally been attributed to protein properties, including binding affinities, abundance, and protein-protein interactions. Following this logic, competition for LD association has generally been described in terms of competition and crowding based on relative binding affinities (67, 68). However, there is growing recognition of LD heterogeneity—encompassing differences in neutral lipid composition which can drive protein targeting. Understanding how MLX selectively interacts with LDs, particularly in the context of this heterogeneity, provides valuable insights into its regulatory mechanisms and broader implications for CYToLD proteins, which leverage conserved AHs for targeting. This work addresses the specific roles of conserved residues within the MLX DCD region, the mechanisms driving its preference for TG-rich over SE-rich LDs, the molecular features enabling stable binding, and the impact of protein association on LD monolayer properties and organization.

We demonstrate that MLX's association mechanism is distinct from other CYToLD proteins, like CCTα and CGI-58, despite all three featuring CYToLD AHs. CCTα binds to expanding LDs via Trp residues that interact with TG-glycerol defects. CGI-58, on the other hand, employs three Trp residues to penetrate deep within LD packing defects (21, 69). MLX sets itself apart by preferentially targeting superficial defects, demonstrating a versatile membrane-binding capacity especially adept at engaging shallow PL defects (Figures 3 b-d, 4 a-f). The selection of shallow defects can be partially explained by the sequence of AH1, which is rich in Leu, Val, and Ile, with strategically positioned Arg, Lys, Phe

and Tyr residues that facilitate membrane surface interactions. Additionally, AH2, enriched with Phe residues, also supports shallow interactions with PL-acyl tail defects. The attraction to shallow defects could also be a consequence of both AH1 and AH2 forming the DCD dimer interface since the smaller hydrophobic residues (Leu, Val, Ile) with larger, aromatic Phe residues allows for a compact dimer alignment (Figure 1). Interestingly, the structure of the DCD when bound to TG-rich LDs closely resembles its conformation in the dimerized state (Figures 1 and 5). This structural overlap suggests that MLX has evolved a dual-functional DCD capable of toggling between dimerization and LD association based on the cellular context, as the compact alignment of smaller hydrophobic residues (Leu, Val, Ile) alongside larger aromatic Phe residues facilitates both dimer formation and stable LD binding. Notably, the specific arrangement of these residues is pivotal, as it not only stabilizes the dimer interface but also primes MLX for its shallow membrane interactions. The ability of the DCD to mimic its dimerized structure while associating with the LD monolayer may enable MLX to dynamically respond to the relative abundance of dimerization partners versus TG-rich LDs, fine-tuning its activity and localization. In contrast, other CYToLD proteins like CCTα and CGI-58, which rely on deeper penetration into LD defects via Trp residues, may be inherently tuned to engage more pronounced membrane perturbations, underscoring a fundamentally different approach to LD recognition.

The specific targeting of MLX to TG-rich LDs is also clear from the thermodynamics of association. Biased simulations verify that both the MLX-hairpin and MLX-DCD exhibit a pronounced thermodynamic preference for TG-rich LDs over the cytosol. The association free energy is approximately -12 kcal/mol for the MLX-hairpin (Figure 6) and -19 kcal/mol for MLX-DCD. Notably, MLX-DCD, at 63 residues in length, displays particularly high stability when bound to the LD, underscoring the robust nature of its interaction with packing defects. Its larger size compared to the MLX-hairpin likely contributes to the greater binding free energy. Additionally, MLX-DCD induces a defect of 92 $Å^2$ upon association, a feature that may explain its specificity for TG-LDs, as defects of this magnitude are rarely observed in bilayers or SE-LD membrane environments (18, 20). Even the MLX-hairpin, which lacks the TG-LD binding specificity of the DCD, experiences a 4 kcal/mol cost for association (Figure 6 a, Movie 3). This cost is attributed to the absence of packing defects on the SE-rich LD monolayer. Experimental work, along with simulations, has shown that SE-rich LDs can undergo a liquid crystalline phase transition (18, 19, 22). Our previous work demonstrated that this transition significantly impacts the PL monolayer, leading to increased ordering of the PLs, reduced area per PL, and decreased packing defects (18). Collectively, these observations highlight how the intrinsic membrane properties of TG-rich LDs drive the preferential binding of MLX.

Turning to the mechanism of association, although there are multiple binding pathways, there is a consistent progression from an initial catch to the gradual burial of hydrophobic residues into packing defects. Both sequences display multiple catch residues on AH1, including an Arg or Lys interaction with PL phosphates (Figures 4, S4 a-c), or alternatively Phe and Tyr residues engaging with PL-acyl defects or hydrogen bonding with PL oxygens (Figures 4). The catch residues facilitate the snorkeling of conserved hydrophobic residues (Leu/Val/Leu/Leu) high in the membrane surface before embedding lower into membrane defects (Figure 7 b-c). The prevalence of an initial catch phase suggests that kinetics will also influence competition since proteins with longer catch phase lifetimes will be selected over those with shorter. Similarly, monolayers with more frequent defect formation will be selected by a given protein over those with less frequent. Additionally, multiple binding pathways enabled by multiple catch residues clearly enhances MLX's affinity; this not only increases the surface states that MLX can engage with but also increases the probability that a second catch, herein called anchoring, can maintain association, further facilitating hydrophobic burial or retaining association if the first catch interaction is lost. Collectively, MLX displays a range of association pathways, utilizing multiple catch residues strategically located at opposing ends of AH1 followed by hydrophobic burial (Movies 1, 2, 4). In addition to protein-membrane interactions, interhelical interactions increase membrane affinity by opposing dissociation. Upon binding, the MLX-hairpin and MLX-DCD settle into stable bound structures (Figures 8 a-e and 7). The MLX-hairpin locks into a specific interhelical tilt angle (Figures 8 d) due to protein-protein hydrogen bonds and hydrophobic contacts (Figures 8 f and S12 a-d). The bound conformation inhibits detachment, echoing findings by Schaefer *et al.* in the SARS-CoV-2 Fusion Peptide, which showed similar interactions bolstering membrane affinity (63). Such interhelical interactions essentially act like glue between two surface-associated cylinders. It is easier to pull either cylinder off in isolation because once glued, pulling one is opposed by the association of the other. Put in the context of stochastic condensed phase dynamics, the statistics of both dissociating together is far less frequent than the

dissociation of either in isolation. Accordingly, MLX's interhelical interactions play a key role increasing membrane affinity and decreasing dissociation rates, consistent with MLX's slow observed off-rate (6). These consistent structural features suggest that the bound conformation is not only thermodynamically stable but also kinetically persistent across conditions and replicates. Our results demonstrate that MLX binding can be reliably characterized using RMSD and end-to-end distance alone (Figure S11 b), as these metrics consistently distinguish the bound conformation from intermediate and unbound states. As such, they serve as effective collective variables for capturing membrane association, and the associated conformational changes may play a role in enabling or enhancing the protein's functional activation at the LD surface. These findings are broadly relevant to other CYToLD proteins, which likely also utilize their own catch residues and conformational changes to target LD monolayers.

Lastly, the binding of the MLX-hairpin and MLX-DCD are shown to alter the physical properties of the surrounding LD monolayer. Although a large packing defect is necessarily formed underneath the protein segments, there is a notable reduction in both the size and number of defects surrounding the protein (> 1-nm away) (Figure 9). This reduction coincides with fewer SURF-TGs on the protein-bound leaflet and an increase in PL tail order parameters, leading to a more ordered lipid membrane beyond 1 nm from the proteins' boundaries (Figures 10 a-c, S14 a-b). Additionally, there is a 34.2% reduction in lateral diffusion coefficients for POPC, showcasing diminished fluidity in the protein-bound leaflet (Figures 10 d-e, SI Table 1). These findings align with broader experimental evidence that demonstrated AH binding to lipid bilayers can enhance adjacent leaflet order, potentially influencing membrane curvature and scission processes (70, 71). Our study extends such protein-induced surface effects to LD monolayers. These altered properties could influence the co-localization of other MLX proteins, which could play an important role in blocking dimerization and dissociation. Alternatively, they could influence the proximal association of other proteins requiring either large packing defects or a direct interaction with surface-active TG.

Conclusions

In summary, this work reveals that MLX targets TG-rich LDs specifically by demanding large packing defects, though it does so distinctly from other CYToLD mechanisms described to date by interacting with shallow PL-acyl defects. These shallow interactions strongly mimic the competing MLX dimer interface, resulting in nearly identical bound poses, whether MLX is bound to a LD monolayer or dimer partner. The specificity for TG-rich LDs and expulsion from SE-rich LDs links lipid metabolic conditions with a transcriptionally regulated glucose metabolism response. We have also characterized the association of a shorter MLX sequence, the MLX-hairpin, that could be useful in targeting membranes more broadly and provides insight to CYtoLD binding mechanisms. Investigating MLX and MYC-like protein localization via leucine zippers attached to the MLX hairpin or MLX DCD could be an interesting research direction.

The mechanism and impacts of LD association described herein suggest that the mechanisms that regulate the LD proteome are likely more nuanced than competing binding affinities alone. The catch, anchor, burial mechanism described for the hairpin suggests that kinetic selection may play a role since the catch phase coupled to the slower formation of packing defects would endow protein selection for systems with longer, more robust catch phases. Indeed, MLX has multiple catch residues strategically placed at opposite ends of the hairpin. Additionally, the interhelical interactions enabled by membrane association disfavor dissociation, imparting increased affinity and slow off rates. Lastly, the altered surface properties proximal to the bound MLX-hairpin and MLX DCD suggest that protein-surface-protein allostery may also influence which proteins bind to LDs and the nature of their colocalization on LD surfaces.

References

1. Zhang, C., and P. Liu. 2019. The New Face of the Lipid Droplet: Lipid Droplet Proteins. *Proteomics*. 19.

2. Olarte, M.J., J.M.J. Swanson, T.C. Walther, and R. V. Farese. 2021. The CYTOLD and ERTOLD pathways for lipid droplet–protein targeting. *Trends Biochem Sci*.

3. Peterson, C.W.H., K.K. Deol, M. To, and J.A. Olzmann. 2021. Optimized protocol for the identification of lipid droplet proteomes using proximity labeling proteomics in cultured human cells. *STAR Protoc*. 2.

4. Walther, T.C., J. Chung, and R. V Farese. 2017. Lipid Droplet Biogenesis. *Annu Rev Cell Dev Biol*.

5. Bersuker, K., and J.A. Olzmann. 2017. Establishing the lipid droplet proteome: Mechanisms of lipid droplet protein targeting and degradation. *Biochim Biophys Acta Mol Cell Biol Lipids*. 1862:1166–1177.

6. Mejhert, N., L. Kuruvilla, K.R. Gabriel, S.D. Elliott, M.A. Guie, H. Wang, Z.W. Lai, E.A. Lane, R. Christiano, N.N. Danial, R. V. Farese, and T.C. Walther. 2020. Partitioning of MLX-Family Transcription Factors to Lipid Droplets Regulates Metabolic Gene Expression. *Mol Cell*. 77:1251-1264.e9.

7. Sans, C.L., D.J. Satterwhite, C.A. Stoltzman, K.T. Breen, and D.E. Ayer. 2006. MondoA-Mlx Heterodimers Are Candidate Sensors of Cellular Energy Status: Mitochondrial Localization and Direct Regulation of Glycolysis. *Mol Cell Biol*. 26:4863–4871.

8. Taniguchi, M., K. Sasaki-Osugi, M. Oku, S. Sawaguchi, S. Tanakura, Y. Kawai, S. Wakabayashi, and H. Yoshida. 2016. MLX Is a Transcriptional Repressor of the Mammalian Golgi Stress Response. .

9. Meroni, G., S. Cairo, G. Merla, S. Messali, R. Brent, A. Ballabio, and A. Reymond. Mlx, a new Max-like bHLHZip family member: the center stage of a novel transcription factors regulatory pathway? .

10. Kawaguchi, T., M. Takenoshita, T. Kabashima, and K. Uyeda. 2001. Glucose and cAMP regulate the L-type pyruvate kinase gene by phosphorylationdephosphorylation of the carbohydrate response element binding protein. .

11. Ma, L., N.G. Tsatsos, and H.C. Towle. 2005. Direct role of ChREBP·Mlx in regulating hepatic glucose-responsive genes. *Journal of Biological Chemistry*. 280:12019–12027.

12. Stoltzman, C.A., C.W. Peterson, K.T. Breen, D.M. Muoio, A.N. Billin, and D.E. Ayer. 2008. Glucose sensing by MondoA:Mlx complexes: A role for hexokinases and direct regulation of thioredoxin-interacting protein expression. .

13. Abdul-Wahed, A., S. Guilmeau, and C. Postic. 2017. Sweet Sixteenth for ChREBP: Established Roles and Future Goals. *Cell Metab*. 26:324–341.

14. Richards, P., S. Ourabah, J. Montagne, A.F. Burnol, C. Postic, and S. Guilmeau. 2017. MondoA/ChREBP: The usual suspects of transcriptional glucose sensing; Implication in pathophysiology. *Metabolism*. 70:133–151.

15. Uyeda, K., and J.J. Repa. 2006. Carbohydrate response element binding protein, ChREBP, a transcription factor coupling hepatic glucose utilization and lipid synthesis. *Cell Metab*. 4:107–110.

16. Peterson, C.W.H., K.K. Deol, M. To, and J.A. Olzmann. 2021. Optimized protocol for the identification of lipid droplet proteomes using proximity labeling proteomics in cultured human cells. *STAR Protoc*. 2.

17. Roberts, M.A., and J.A. Olzmann. 2020. Protein Quality Control and Lipid Droplet Metabolism. *Annu Rev Cell Dev Biol*. 36:115–139.

18. Braun, R.J., and J.M.J. Swanson. 2022. Capturing the Liquid-Crystalline Phase Transformation: Implications for Protein Targeting to Sterol Ester-Rich Lipid Droplets. *Membranes (Basel)*. 12.

19. Rogers, S., L. Gui, A. Kovalenko, V. Zoni, M. Carpentier, K. Ramji, K. Ben Mbarek, A. Bacle, P. Fuchs, P. Campomanes, E. Reetz, N.O. Speer, E. Reynolds, A.R. Thiam, S. Vanni, D. Nicastro, and W. Mike Henne. 2022. Triglyceride lipolysis triggers liquid crystalline phases in lipid droplets and alters the LD proteome. *Journal of Cell Biology*. 221.

20. Kim, S., and J.M.J. Swanson. 2020. The Surface and Hydration Properties of Lipid Droplets. *Biophys J*. 119:1958–1969.

21. Kim, S., M.I. Oh, and J.M.J. Swanson. 2021. Stressed Lipid Droplets: How Neutral Lipids Relieve Surface Tension and Membrane Expansion Drives Protein Association. *Journal of Physical Chemistry B*. 125:5572–5586.

22. Mahamid, J., D. Tegunov, A. Maiser, J. Arnold, H. Leonhardt, J.M. Plitzko, and W. Baumeister. 2019. Liquid-crystalline phase transitions in lipid droplets are related to cellular states and specific organelle association. *Proc Natl Acad Sci U S A*. 116:16866–16871.

23. Speer, N.O., R.J. Braun, E.G. Reynolds, A. Brudnicka, J.M.J. Swanson, and W.M. Henne. 2024. Tld1 is a regulator of triglyceride lipolysis that demarcates a lipid droplet subpopulation. *J Cell Biol*. 223.

24. Chorlay, A., and A.R. Thiam. 2020. Neutral lipids regulate amphipathic helix affinity for model lipid droplets. *Journal of Cell Biology*. 219.

25. Olarte, M.J., S. Kim, M.E. Sharp, J.M.J. Swanson, R. V. Farese, and T.C. Walther. 2020. Determinants of Endoplasmic Reticulum-to-Lipid Droplet Protein Targeting. *Dev Cell*. 54:471-487.e7.

26. Kim, S., J.M.J. Swanson, and G.A. Voth. 2022. Computational Studies of Lipid Droplets. *Journal of Physical Chemistry B*. 126:2145–2154.

27. Czabany, T., A. Wagner, D. Zweytick, K. Lohner, E. Leitner, E. Ingolic, and G. Daum. 2008. Structural and biochemical properties of lipid particles from the yeast Saccharomyces cerevisiae. *Journal of Biological Chemistry*. 283:17065–17074.

28. Khor, V.K., R. Ahrends, Y. Lin, W.J. Shen, C.M. Adams, A.N. Roseman, Y. Cortez, M.N. Teruel, S. Azhar, and F.B. Kraemer. 2014. The proteome of cholesteryl-ester-enriched versus triacylglycerol-enriched lipid droplets. *PLoS One*. 9.

29. Brooks, B.R., C.L. Brooks, A.D. Mackerell, L. Nilsson, R.J. Petrella, B. Roux, Y. Won, G. Archontis, C. Bartels, S. Boresch, A. Caflisch, L. Caves, Q. Cui, A.R. Dinner, M. Feig, S. Fischer, J. Gao, M. Hodoscek, W. Im, K. Kuczera, T. Lazaridis, J. Ma, V. Ovchinnikov, E. Paci, R.W. Pastor, C.B. Post, J.Z. Pu, M. Schaefer, B. Tidor, R.M. Venable, H.L. Woodcock, X. Wu, W. Yang, D.M. York, and M. Karplus. 2009. CHARMM: The biomolecular simulation program. *J Comput Chem*. 30:1545–1614.

30. Huang, J., S. Rauscher, G. Nawrocki, T. Ran, M. Feig, B.L. De Groot, H. Grubmüller, and A.D. MacKerell. 2016. CHARMM36m: An improved force field for folded and intrinsically disordered proteins. *Nat Methods*. 14:71–73.

31. Campomanes, P., J. Prabhu, V. Zoni, and S. Vanni. 2021. Recharging your fats: CHARMM36 parameters for neutral lipids triacylglycerol and diacylglycerol. *Biophysical Reports*. 1:100034.

32. Kim, S., and G.A. Voth. 2021. Physical Characterization of Triolein and Implications for Its Role in Lipid Droplet Biogenesis. *J Phys Chem B*. 125:6874–6888.

33. Chorlay, A., L. Forêt, and A.R. Thiam. 2021. Origin of gradients in lipid density and surface tension between connected lipid droplet and bilayer. *Biophys J*. 120:5491–5503.

34. Braun, R.J., and J.M.J. Swanson. 2025. Progress in Lipid Droplet Simulations: How Polarizability Shapes Triacylglycerol Behavior in Bulk and Interfacial Environments. *submitted for publication*.

35. Jo, S., T. Kim, V.G. Iyer, and W. Im. 2008. CHARMM-GUI: A web-based graphical user interface for CHARMM. *J Comput Chem*. 29:1859–1865.

36. Jo, S., J.B. Lim, J.B. Klauda, and W. Im. 2009. CHARMM-GUI membrane builder for mixed bilayers and its application to yeast membranes. *Biophys J*. 97:50–58.

37. Lee, J., X. Cheng, J.M. Swails, M.S. Yeom, P.K. Eastman, J.A. Lemkul, S. Wei, J. Buckner, J.C. Jeong, Y. Qi, S. Jo, V.S. Pande, D.A. Case, C.L. Brooks, A.D. MacKerell, J.B. Klauda, and W. Im. 2016. CHARMM-GUI Input Generator for NAMD, GROMACS, AMBER, OpenMM, and CHARMM/OpenMM Simulations Using the CHARMM36 Additive Force Field. *J Chem Theory Comput*. 12:405–413.

38. Yang, Y., M. Lee, and G.D. Fairn. 2018. Phospholipid subcellular localization and dynamics. *Journal of Biological Chemistry*. 293:6230–6240.

39. Klauda, J.B., R.M. Venable, J.A. Freites, J.W. O'Connor, D.J. Tobias, C. Mondragon-Ramirez, I. Vorobyov, A.D. MacKerell, and R.W. Pastor. 2010. Update of the CHARMM All-Atom Additive Force Field for Lipids: Validation on Six Lipid Types. *Journal of Physical Chemistry B*. 114:7830–7843.

40. Venable, R.M., A.J. Sodt, B. Rogaski, H. Rui, E. Hatcher, A.D. MacKerell, R.W. Pastor, and J.B. Klauda. 2014. CHARMM all-atom additive force field for sphingomyelin: Elucidation of hydrogen bonding and of positive curvature. *Biophys J*. 107:134–145.

41. Jorgensen, W.L., J. Chandrasekhar, J.D. Madura, R.W. Impey, and M.L. Klein. 1983. Comparison of simple potential functions for simulating liquid water. *J Chem Phys*. 79:926–935.

42. Abraham, M.J., T. Murtola, R. Schulz, S. Páll, J.C. Smith, B. Hess, and E. Lindah. 2015. Gromacs: High performance molecular simulations through multi-level parallelism from laptops to supercomputers. *SoftwareX*. 1–2:19–25.

43. Nosé, S. 1984. A unified formulation of the constant temperature molecular dynamics methods. *J Chem Phys*. 81:511–519.

44. Hoover, W.G. 1985. Canonical dynamics: Equilibrium phase-space distributions. .

45. Essmann, U., L. Perera, M.L. Berkowitz, T. Darden, H. Lee, and L.G. Pedersen. 1995. A smooth particle mesh Ewald method. *J Chem Phys*. 103:8577–8593.

46. Parrinello, M., and A. Rahman. 1981. Polymorphic transitions in single crystals: A new molecular dynamics method. *J Appl Phys*. 52:7182–7190.

47. Hess, B. 2008. P-LINCS: A parallel linear constraint solver for molecular simulation. *J Chem Theory Comput*. 4:116–122.

48. Humphrey, W., A. Dalke, and K. Schulten. 1996. VMD: Visual Molecular Dynamics. .

49. Gowers, R.J., M. Linke, J. Barnoud, T.J. E Reddy, M.N. Melo, S.L. Seyler, J. Domá nski, D.L. Dotson, S. Buchoux, I.M. Kenney, and O. Beckstein. 2016. MDAnalysis: A Python Package for the Rapid Analysis of Molecular Dynamics Simulations. .

50. Barber, C.B., and D.P. Dobkin. 1996. The Quickhull Algorithm for Convex Hulls. .

51. Gautier, R., A. Bacle, M.L. Tiberti, P.F. Fuchs, S. Vanni, and B. Antonny. 2018. PackMem: A Versatile Tool to Compute and Visualize Interfacial Packing Defects in Lipid Bilayers. *Biophys J*. 115:436–444.

52. Prévost, C., M.E. Sharp, N. Kory, Q. Lin, G.A. Voth, R. V. Farese, and T.C. Walther. 2018. Mechanism and Determinants of Amphipathic Helix-Containing Protein Targeting to Lipid Droplets. *Dev Cell*. 44:73-86.e4.

53. Cui, H., E. Lyman, and G.A. Voth. 2011. Mechanism of membrane curvature sensing by amphipathic helix containing proteins. *Biophys J*. 100:1271–1279.

54. Schindler, H., and J. Seelig. 1975. Deuterium Order Parameters in Relation to Thermodynamic Properties of a Phospholipid Bilayer. A Statistical Mechanical Interpretation^. .

55. de Buyl, P. 2018. tidynamics: A tiny package to compute the dynamics of stochastic and molecular simulations. *J Open Source Softw*. 3:877.

56. Calandrini, V., E. Pellegrini, P. Calligari, K. Hinsen, and G.R. Kneller. 2011. nMoldyn - Interfacing spectroscopic experiments, molecular dynamics simulations and models for time correlation functions. *École thématique de la Société Française de la Neutronique*. 12:201–232.

57. Izrailev, S., S. Stepaniants, B. Isralewitz, D. Kosztin, H. Lu, F. Molnar, W. Wriggers, and K. Schulten. 1999. Steered Molecular Dynamics. In: Deuflhard P, J Hermans, B Leimkuhler, AE Mark, S Reich, RD Skeel, editors. Computational Molecular Dynamics: Challenges, Methods, Ideas. Berlin, Heidelberg: Springer Berlin Heidelberg. pp. 39–65.

58. Aydin, F., A.E.P. Durumeric, G.C.A. da Hora, J.D.M. Nguyen, M.I. Oh, and J.M.J. Swanson. 2021. Improving the accuracy and convergence of drug permeation simulations via machine-learned collective variables. *Journal of Chemical Physics*. 155.

59. da Hora, G.C.A., J.D.M. Nguyen, and J.M.J. Swanson. 2022. Can membrane composition traffic toxins? Mycolactone and preferential membrane interactions. *Biophys J*. 121:4260–4270.

60. Torrie, G.M., and J.P. Valleau. 1974. Monte Carlo free energy estimates using non-Boltzmann sampling: Application to the sub-critical Lennard-Jones fluid. *Chem Phys Lett*. 28:578–581.

61. Hub, J.S., B.L. De Groot, and D. Van Der Spoel. 2010. G-whams-a free Weighted Histogram Analysis implementation including robust error and autocorrelation estimates. *J Chem Theory Comput*. 6:3713–3720.

62. Sammak, S., N. Hamdani, F. Gorrec, M.D. Allen, S.M.V. Freund, M. Bycroft, and G. Zinzalla. 2019. Crystal Structures and Nuclear Magnetic Resonance Studies of the Apo Form of the c-MYC:MAX bHLHZip Complex Reveal a Helical Basic Region in the Absence of DNA. *Biochemistry*. 58:3144–3154.

63. Schaefer, S.L., H. Jung, and G. Hummer. 2021. Binding of SARS-CoV-2 Fusion Peptide to Host Endosome and Plasma Membrane. *Journal of Physical Chemistry B*. 125:7732–7741.

64. Llombart, V., and M.R. Mansour. 2022. Therapeutic targeting of “undruggable” MYC. .

65. Krahmer, N., M. Hilger, N. Kory, F. Wilfling, G. Stoehr, M. Mann, R. V. Farese, and T.C. Walther. 2013. Protein correlation profiles identify lipid droplet proteins with high confidence. *Molecular and Cellular Proteomics*. 12:1115–1126.

66. Brasaemle, D.L., G. Dolios, L. Shapiro, and R. Wang. 2004. Proteomic analysis of proteins associated with lipid droplets of basal and lipolytically stimulated 3T3-L1 adipocytes. *Journal of Biological Chemistry*. 279:46835–46842.

67. Kory, N., R. V. Farese, and T.C. Walther. 2016. Targeting Fat: Mechanisms of Protein Localization to Lipid Droplets. *Trends Cell Biol*. 26:535–546.

68. Kory, N., A.R. Thiam, R. V. Farese, and T.C. Walther. 2015. Protein Crowding Is a Determinant of Lipid Droplet Protein Composition. *Dev Cell*. 34:351–363.

69. Boeszoermenyi, A., H.M. Nagy, H. Arthanari, C.J. Pillip, H. Lindermuth, R.E. Luna, G. Wagner, R. Zechner, K. Zangger, and M. Oberer. 2015. Structure of a CGI-58 motif provides the molecular basis of lipid droplet anchoring. *Journal of Biological Chemistry*. 290:26361–26372.

70. Ge, M., and J.H. Freed. 2009. Fusion peptide from influenza hemagglutinin increases membrane surface order: An electron-spin resonance study. *Biophys J*. 96:4925–4934.

71. Martyna, A., B. Bahsoun, M.D. Badham, S. Srinivasan, M.J. Howard, and J.S. Rossman. 2017. Membrane remodeling by the M2 amphipathic helix drives influenza virus membrane scission. *Sci Rep*. 7.

Acknowledgements

The authors are grateful for helpful discussions with Robert V Farese and Tobias C. Walther. The work was supported by the National Science Foundation under Grant No. (2341008) and the computational resources provided by Expanse through the San Diego Supercomputer through the Center Advanced Cyberinfrastructure Coordination Ecosystem (ACCESS) program (allocation MCB200018) supported by NSF (grant nos. 2138259, 2138286, 2138307, 2137603, and 2138296), as well as the Center for High-Performance Computing (CHPC) at the University of Utah. These resources greatly aided in the completion of this research.

Author contributions

R.J.B and J.M.J.S designed the research. R.J.B. ran the simulations and analyzed the results. J.M.J.S directed the research. Both authors wrote the manuscript and agreed on the final version.

Competing interests

The authors declare no competing interests.